JOTCSA
Journal of the Turkish Chemical Society Section: A Chemistry
TURKISH CHEMICAL SOCIETY

Structural, Microstructural, and Dielectric Insights into Eu^{3+}-Doped and Eu^{3+}, B^{3+} Co-Doped Sr_2GdTaO_6 Double Perovskite Ceramics

Mustafa İlhan[1*], Lütfiye Feray Güleryüz[2], Mehmet İsmail Katı[3]

[1]Department of Jewelry and Jewelry Design, Faculty of Applied Sciences, Marmara University, Kartal, 34865, İstanbul, Türkiye.
[2]Department of Automotive Engineering, Faculty of Technology, Kocaeli University, 41001, Kocaeli, Türkiye.
[3]Department of Medical Imaging Techniques, Vocational School of Health Sciences, Manisa Celal Bayar University, 45030, Manisa, Türkiye.

Abstract: The structural, microstructural, and dielectric properties of Eu^{3+}-doped and Eu^{3+}, B^{3+} co-doped Sr_2GdTaO_6 double perovskite ceramics were systematically investigated. X-ray diffraction (XRD) analysis confirmed that all samples crystallize in the monoclinic $P2_1/n$ space group with long-range B/B′ ordering, remaining single-phase up to 20 mol% Eu^{3+} and 70 mol% B^{3+}. The peak-shift analysis revealed a slight shift toward lower angles, attributed to the substitution of Gd^{3+} by Eu^{3+} and the indirect structural perturbations induced by boron incorporation through charge compensation and microstrain effects. Crystallite sizes, derived from Scherrer and Williamson–Hall analyses, were found in the 30–45 nm range, with microstrain and defect densities increasing under Eu^{3+} doping but significantly reduced at moderate B^{3+} contents, consistent with the fluxing effect of boron. Scanning electron microscopy (SEM) revealed dense, terraced grains of 4–13 μm in the Eu^{3+} series, while boron addition promoted grain growth up to ~25 μm and faceted morphologies at intermediate concentrations. Excessive boron, however, yielded heterogeneous microstructures and secondary phases, aligning with XRD observations. Dielectric measurements demonstrated frequency-dependent behavior consistent with the Maxwell–Wagner model. For the Eu^{3+} series, the dielectric constant decreased from 32.4 to 21.8 at 20 Hz with increasing Eu^{3+}, reflecting reduced crystallinity and enhanced microstrain. In contrast, moderate boron addition significantly enhanced the dielectric constant (up to 45.7 at 20 Hz) and suppressed dielectric loss, owing to improved densification, larger grains, and reduced oxygen-vacancy-related conduction. At high boron contents (70 and 100 mol%), both ε' and tan δ degraded, attributed to strain accumulation and secondary phase formation. These results establish clear correlations between defect chemistry, microstructure, and dielectric response in Sr_2GdTaO_6 ceramics, highlighting the potential of controlled Eu^{3+} substitution and optimized boron co-doping for tailoring multifunctional dielectric materials.

Keywords: Double perovskite ceramics; Eu^{3+} doping; Boron co-doping; Dielectric properties; Microstructure–property correlation.

Submitted: September 24, 2025. **Accepted:** January 21, 2026.

Cite this: İlhan M, Güleryüz LF, Katı MI. Structural, Microstructural, and Dielectric Insights into Eu^{3+}-Doped and Eu^{3+}, B^{3+} Co-Doped Sr_2GdTaO_6 Double Perovskite Ceramics. JOTCSA. 2026, **1790637**, 1-15.

DOI: https://doi.org/10.18596/jotcsa.1790637

***Corresponding author's E-mail:** mustafa.ilhan@marmara.edu.tr

1. INTRODUCTION

Perovskite oxides with the general formula ABO_3, in which the A and B sites are occupied by different cations, exhibit remarkable structural stability owing to the balanced arrangement of constituent ions and their valences. The inherent flexibility of the perovskite lattice allows a wide range of chemical substitutions, leading to the emergence of a novel family of compounds known as double perovskite oxides (1–6). These materials, typically expressed by the formula $A_2BB'O_6$, are formed when the B site of the parent ABO_3 lattice is alternately occupied by two distinct cations—commonly rare-earth ions (B) and transition metals (B′ = Nb, Ta, Mo, Sb, etc.)—which may be either ordered or disordered (7,8). Owing to this compositional versatility, double perovskites incorporating alkali or rare-earth ions at the A-site and transition-metal cations at the B/B′ sites have

attracted significant scientific attention (9,10). Their diverse functional properties, such as dielectric response, ferroelectricity, magnetism, and luminescence, make them promising candidates for technological applications (11,12).

The incorporation of rare-earth elements into ceramic hosts further enhances their functional versatility, imparting unique electrical, optical, magnetic, and catalytic characteristics (13,14). Within $A_2BB'O_6$ structures, the corner-sharing BO_6 and $B'O_6$ octahedra may distort the local symmetry at the A-site, thereby creating favorable environments for accommodating luminescent rare-earth ions (15–20). Among these, trivalent europium (Eu^{3+}) has attracted particular interest due to its intense red emission, arising from the sharp $^5D_0 \rightarrow {}^7F_J$ (J = 0–6) transitions. The non-degenerate nature of the $^5D_0$ state results in well-resolved absorption and emission features, making Eu^{3+} an excellent probe ion for investigating structure–property correlations and a reliable activator for optoelectronic applications (21–28). On the other hand, boron-based additives (commonly introduced via H_3BO_3) are extensively used as flux agents in solid-state synthesis, owing to their relatively low melting temperature. Boron not only promotes densification and grain growth during sintering but can also influence the microstructure, optical, and dielectric behavior of ceramics (29–34). Previous studies indicate that B-addition can reduce porosity, modify grain morphology, and enhance bulk dielectric properties by minimizing grain-boundary effects (33–37).

In this context, the present work focuses on Eu^{3+}-doped and Eu^{3+}, B^{3+} co-doped Sr_2GdTaO_6 ceramics, systematically comparing their structural and dielectric characteristics. The crystallite size and microstrain were evaluated by the Scherrer and Williamson–Hall (W–H) methods, while the microstructural features were examined by scanning electron microscopy (SEM). The dielectric properties were investigated using impedance spectroscopy over a wide frequency range. This study builds upon our previous report on the structural and spectral characteristics of Sr_2GdTaO_6-based phosphors (8), extending the analysis toward a deeper understanding of the interplay between structure, microstructure, and dielectric performance. Unlike earlier studies that mainly explored the optical or luminescent characteristics of Sr_2GdTaO_6-based materials, the present work focuses on the correlation between lattice distortion, defect chemistry, and frequency-dependent dielectric response. The combined Eu^{3+} substitution and B^{3+} co-doping strategy has not been previously reported for this host, particularly regarding flux-assisted microstructural evolution and its quantitative impact on dielectric enhancement. This study therefore addresses the existing scientific gap by establishing how Eu^{3+} incorporation and boron-induced densification jointly modify crystallinity, defect density, and charge-transport behavior. Accordingly, it introduces a new compositional pathway for optimizing dielectric performance in rare-earth-modified double perovskites through simultaneous control of lattice order, microstructure, and defect chemistry.

2. EXPERIMENTAL

$Sr_2Gd_{1-x}TaO_6$:xEu^{3+} (x =0, 0.5, 1.5, 3, 5, 7, 10, 20 mol%) and $Sr_2Gd_{1-x}TaO_6$:xEu^{3+}, yB^{3+} (x=10 mol%, y=0, 5, 15, 30, 50, 70, 100 mol%) ceramic series were fabricated by solid-state method. Strontium carbonate ($SrCO_3$, Sigma-Aldrich, 99%), tantalum oxide (Ta_2O_5, Alpha Aesar, 99.9%), and gadolinium oxide (Gd_2O_3, Alpha Aesar, 99.9%) powders were employed as the primary materials in stoichiometric proportions. Europium oxide (Eu_2O_3, Alpha Aesar, 99.9%) and boric acid (H_3BO_3, Kimyalab, 99.9%) served as doping agents. The starting materials for $Sr_2Gd_{1-x}Eu_xTaO_6$ ($SrCO_3$+Ta_2O_5 + (1-x)Gd_2O_3 + $x$$Eu_2O_3$) and $Sr_2Gd_{0.9}Eu_{0.1}TaO_6$ ($SrCO_3$ + Ta_2O_5 + $0.9Gd_2O_3$+ $0.1Eu_2O_3$) series were weighed and mixed in an agate mortar using the required stoichiometric quantities. For $Sr_2Gd_{0.9}Eu_{0.1}TaO_6$ series different amounts of boric acid (H_3BO_3) was added. The final powder mixtures for the series were thoroughly blended in an agate mortar to achieve a uniform composition. For the sintering process, the samples were placed in alumina crucibles after the pelleting process and calcined at 1350 °C for 6 h.

The phase composition was analyzed by X-ray diffraction (XRD; Panalytical Emperial, Malvern Panalytical Ltd., United Kingdom) using Cu-K_α (1.5406 Å) radiation in between 2θ=20-70 (°) with scan speed 2 °/min. The crystal structure was depicted using VESTA software. The grain structure of the ceramic samples was investigated using a field emission scanning electron microscope (FE-SEM; Gemini 500, Zeiss Corp., Germany). The crystal structure was visualized via VESTA software. The average crystallite sizes of the samples were determined from the Scherrer Eq. (1) (38-40):

$$D = \frac{k \cdot \lambda}{B \cdot cos\,\theta} \quad (1)$$

where D stands for particle size in nanometers, with k is a constant (usually taken as 0.9). CuKα represents the wavelength (λ = 0.15406 Å), and B is the full width at half maximum in radians. Frequency-dependent changes of real and imaginary permittivity and loss factor were defined using dielectric Eq. (2) and Eq. (3) respectively:

$$\varepsilon' = \frac{C}{C_0}, \qquad \varepsilon'' = \frac{G}{\omega C_0}, \qquad C_0 = \varepsilon_0 \frac{A}{d} \quad (2)$$

$$tan\delta = \frac{\varepsilon''}{\varepsilon'} \quad (3)$$

where C_0 is vacuum capacitance, C is capacitance, w is angular frequency and G is conductance. The dielectric properties of the ceramic samples were carried out using an impedance analyzer (HIOKI, LCR Hitester 3532-50; between frequency 20 Hz–10^6 Hz, UK) at room temperature.

3. RESULTS AND DISCUSSION

3.1. XRD-SEM Results of Eu^{3+} Doped and Eu^{3+}, B^{3+} Co-Doped Sr_2GdTaO_6

Figure 1a shows the powder XRD patterns of the $Sr_2Gd_{1-x}Eu_xTaO_6$ series (x = 0–20 mol%). All major reflections are well indexed to the monoclinic double perovskite phase ($P2_1/n$, No. 14), consistent with JCPDS 47-0527 (Sr_2EuTaO_6). No detectable impurity reflections are observed up to x = 0.20, confirming that Eu^{3+} ions are isovalently incorporated at the Gd^{3+} site within the B-sublattice (Gd^{3+}/Ta^{5+} network), preserving the long-range B/B′ ordering. Figure 2a displays the diffraction patterns of $Sr_2Gd_{0.90}Eu_{0.1}TaO_6$:$yB^{3+}$ (y = 0–100 mol%). These remain monophasic up to y = 50 mol%, whereas weak secondary peaks emerge at y = 70 and 100 mol%, indicative of the onset of secondary phases. To further validate the structural interpretation, the diffraction patterns were examined in detail. The absence of extra reflections confirms that all samples retain the monoclinic $P2_1/n$ symmetry. In the Eu^{3+}-doped series, the (020)/($\bar{1}$12)/(200) group around 30.5° and the (220) reflection near 43.9° show a systematic shift toward lower 2θ angles with increasing Eu^{3+} content, indicating gradual lattice expansion caused by the slightly larger ionic radius of Eu^{3+} compared with Gd^{3+} (Figure 1b). Similarly, for the B^{3+}-modified samples, a slight shift of these reflections toward lower 2θ values (Figure 2b) is also observed, suggesting that the peak displacement originates from defect-assisted incorporation and local structural relaxation associated with B^{3+} concentration. In addition, a reduction in peak broadening at moderate B^{3+} levels points to improved crystallinity and decreased microstrain, in agreement with the Williamson–Hall analysis (Tables 1 and 2). Although a full Rietveld refinement was not conducted, the observed peak-shift and profile variations clearly evidence lattice distortion and confirm the preservation of B/B′ ordering within the $P2_1/n$ framework. The perovskite lattice comprises corner-sharing GdO_6 and TaO_6 octahedra (Figure 3). The ionic radii of Ta^{5+} and Gd^{3+} are 0.64 Å and 0.938 Å, respectively, assuming a coordination number (CN) of 6, whereas Sr^{2+} ions occupy the A sites with an ionic radius of 1.26 Å and CN of 8 (6,40). Substitution of Gd^{3+} with slightly larger Eu^{3+} (0.947 Å, CN = 6) is expected to induce local lattice expansion, consistent with the systematic shift of the ($\bar{1}$12) reflection to lower 2θ (Figure 1b). For the B^{3+}-modified samples, the apparent lattice expansion cannot be rationalized by direct Ta/Gd substitution (ionic size and charge incompatibility); rather, it is attributed to flux-mediated defect chemistry, local oxygen nonstoichiometry, and subtle changes in octahedral tilting. Line broadening analysis was performed using both the Scherrer equation and the Williamson–Hall (W–H) method. The Scherrer-derived crystallite sizes (Tables 1 and 2) decrease modestly with Eu^{3+} substitution (from 39.8 nm to 33.3 nm) and vary in the 33.6–38.3 nm range for B^{3+} concentration. However, the Scherrer method assumes that peak broadening arises solely from finite size, neglecting strain effects, which often leads to an underestimation of true crystallite size when microstrain is significant. The W–H method incorporates both size and strain according to Eq. (4) (41–45):

$$\beta cos\theta = \epsilon(4sin\theta) + \frac{\lambda}{D} \quad (4)$$

where β is the full width at half maximum (FWHM), ε is the microstrain, D is the crystallite size, λ is the X-ray wavelength, and θ is the Bragg angle. Linear fits (Figures 4 and 5) yield slightly larger crystallite sizes: 44.9–37.1 nm for Eu^{3+} substitution and 37.3–43.0 nm for B^{3+} co-doping. The intercept provides D (size), while the slope quantifies microstrain (ε). The higher W–H sizes relative to Scherrer confirm that strain broadening contributes measurably to the diffraction peak profiles, which are otherwise treated as size effects alone in the Scherrer approximation (43). The dislocation density (δ) and stacking fault probability (SF) were evaluated using Eqs. (5) and (6) (42):

$$\delta = \frac{1}{D^2} \quad (5)$$

$$SF = [\frac{2\pi^2}{45(3\tan\theta)^{½}}] \times \beta \quad (6)$$

Microstructural parameters derived from W–H and subsequent models are summarized in Tables 1 and 2. The microstrain (ε) increases systematically with Eu^{3+} substitution, rising from 1.95 × 10^{-5} (undoped) to 4.21 × 10^{-5} (x = 0.20). This correlates with enhanced octahedral distortion and local strain fields introduced by size mismatch. The dislocation density (δ), calculated by Eq. (5), rises from ~6.2 × 10^{14} m^{-2} to 9.1 × 10^{14} m^{-2} across the Eu^{3+} series, indicating a higher density of crystallographic defects. Likewise, the stacking fault probability (SF) calculated by Eq. (6), grows slightly with Eu^{3+} addition, reflecting perturbation of long-range order due to substitution-induced strain. In the Eu^{3+}, B^{3+} co-doped series, the trends are non-monotonic. At moderate B^{3+} levels (≤50 mol%), ε, δ, and SF decrease, suggesting that boron promotes flux-assisted crystallization, reduces porosity, and enhances grain coalescence, thereby lowering defect density. However, at higher loadings (≥70 mol% B^{3+}), ε and δ increase again, consistent with XRD detection of secondary phases and SEM evidence of microstructural heterogeneity.

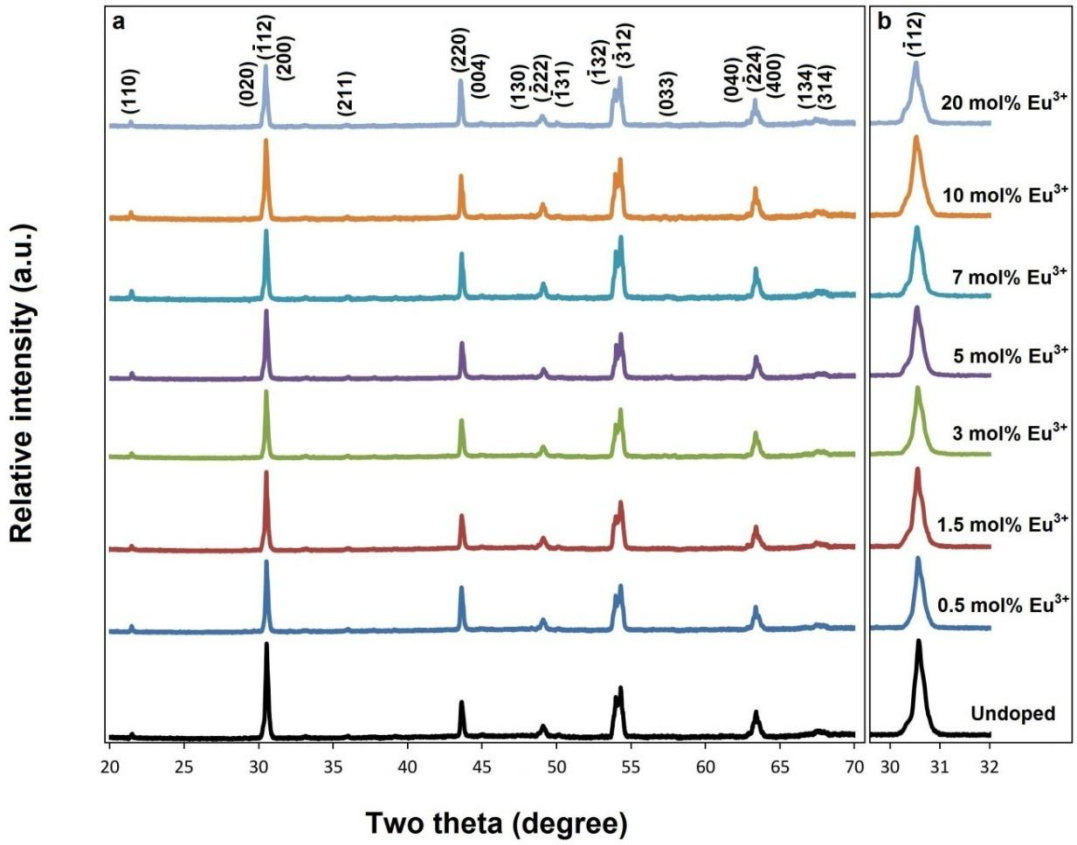

Figure 1: XRD patterns of $Sr_2Gd_{1-x}Eu_xTaO_6$ (x = 0–20 mol%): (a) full diffraction range and (b) enlarged view around the (1̄12) reflection.

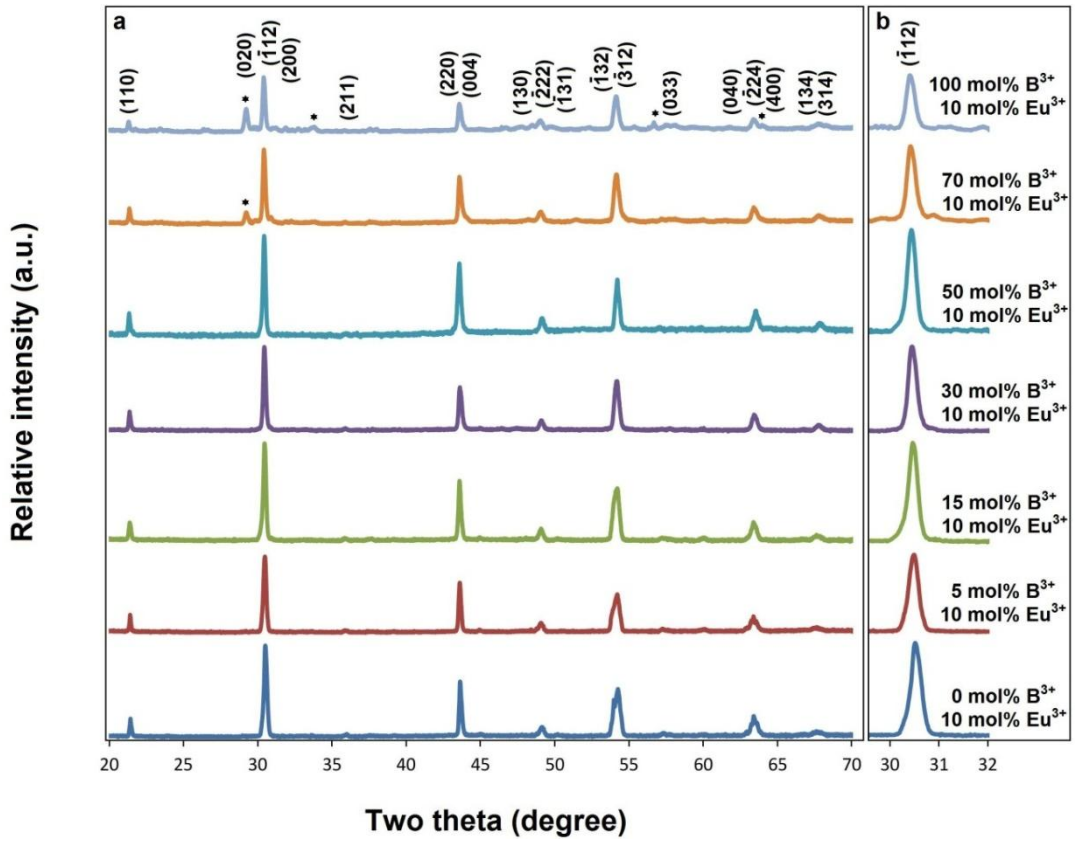

Figure 2: XRD patterns of $Sr_2Gd_{0.9}Eu_{0.1}TaO_6:B^{3+}$ (y = 0–100 mol%): (a) full diffraction range, and (b) magnified region highlighting the (1̄12) reflection.

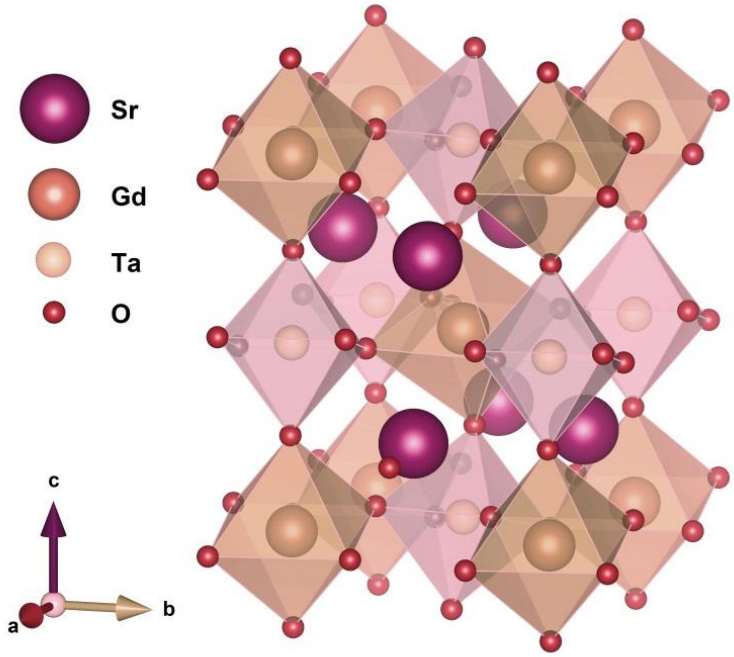

Figure 3: Crystal structure model of Sr_2GdTaO_6 ($P2_1/n$).

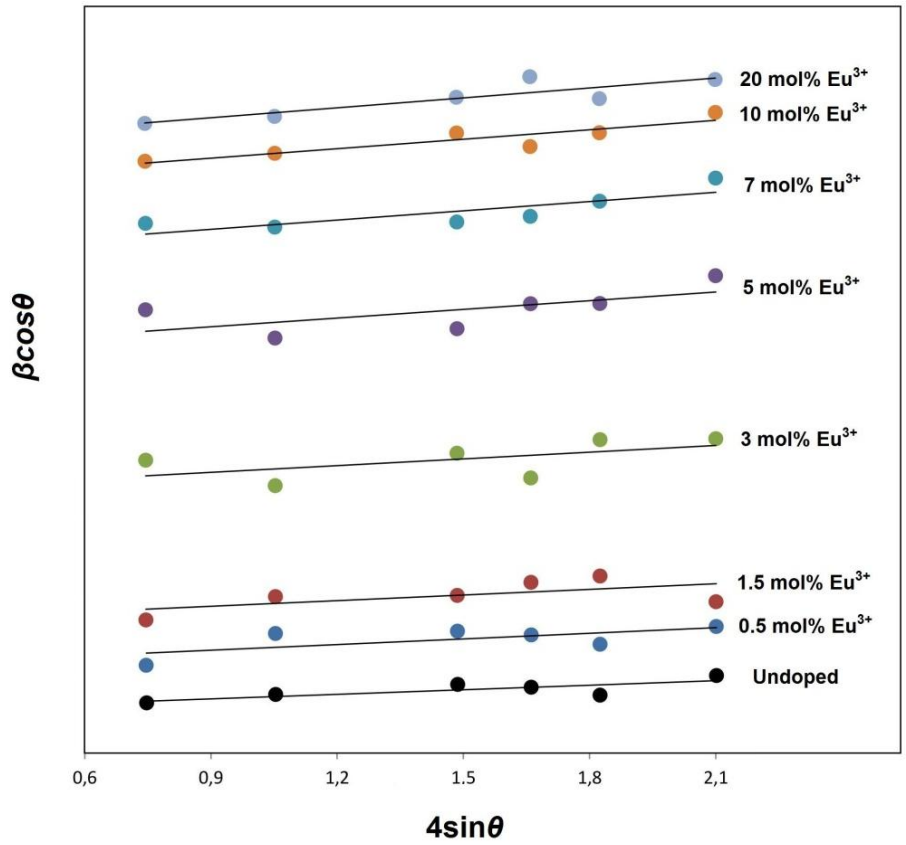

Figure 4: Williamson–Hall plot for $Sr_2Gd_{1-x}Eu_xTaO_6$ (x = 0–20 mol%) ceramics.

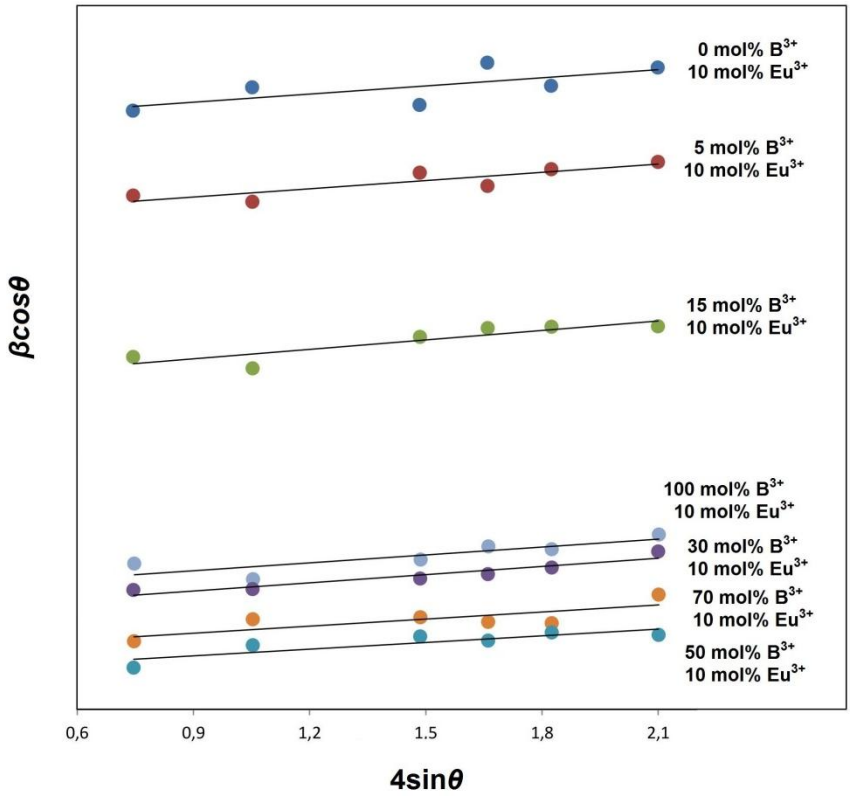

Figure 5: Williamson–Hall plot for $Sr_2Gd_{0.9}Eu_{0.1}TaO_6$:$B^{3+}$ (y = 0–100 mol%) ceramics.

Table 1: Estimated crystallite size, microstrain, dislocation density and stacking fault values for Sr_2GdTaO_6:Eu^{3+} samples.

Eu^{3+} conc. (x mol%)	$Sr_2Gd_{1-x}TaO_6$:xEu^{3+}				
	Crystallite size		Microstrain (ε)	Dislocation density (δ) (m^{-2})	Stacking fault (SF)
	Scherrer (nm)	W-H (nm)			
0	39.8	44.9	1.95×10^{-5}	6.21×10^{14}	1.49×10^{-3}
0.5	39.3	44.2	2.41×10^{-5}	6.49×10^{14}	1.51×10^{-3}
1.5	38.7	43.5	2.39×10^{-5}	6.66×10^{14}	1.54×10^{-3}
3	37.3	41.5	2.86×10^{-5}	7.20×10^{14}	1.63×10^{-3}
5	36.4	40.8	3.78×10^{-5}	7.57×10^{14}	1.65×10^{-3}
7	35.5	39.8	4.00×10^{-5}	7.95×10^{14}	1.69×10^{-3}
10	35.0	39.1	4.21×10^{-5}	8.18×10^{14}	1.72×10^{-3}
20	34.3	38.5	4.71×10^{-5}	8.53×10^{14}	1.75×10^{-3}

Table 2: Estimated crystallite size, microstrain, dislocation density and stacking fault values for Sr_2GdTaO_6:Eu^{3+}, B^{3+} samples.

B^{3+} conc. (y mol%)	$Sr_2Gd_{1-x}TaO_6$:xEu^{3+}, yB^{3+} (x=10 mol%)				
	Crystallite size		Microstrain (ε)	Dislocation density (δ) (m^{-2})	Stacking fault (SF)
	Scherrer (nm)	W-H (nm)			
0	33.6	37.3	3.40×10^{-5}	9.09×10^{14}	1.80×10^{-3}
5	34.7	38.3	3.23×10^{-5}	8.51×10^{14}	1.76×10^{-3}
15	36.0	40.1	3.06×10^{-5}	7.79×10^{14}	1.68×10^{-3}
30	38.6	43.2	2.80×10^{-5}	6.75×10^{14}	1.56×10^{-3}
50	39.3	44.2	2.63×10^{-5}	6.46×10^{14}	1.52×10^{-3}
70	39.0	43.8	2.77×10^{-5}	6.58×10^{14}	1.53×10^{-3}
100	38.3	42.9	2.92×10^{-5}	6.77×10^{14}	1.57×10^{-3}

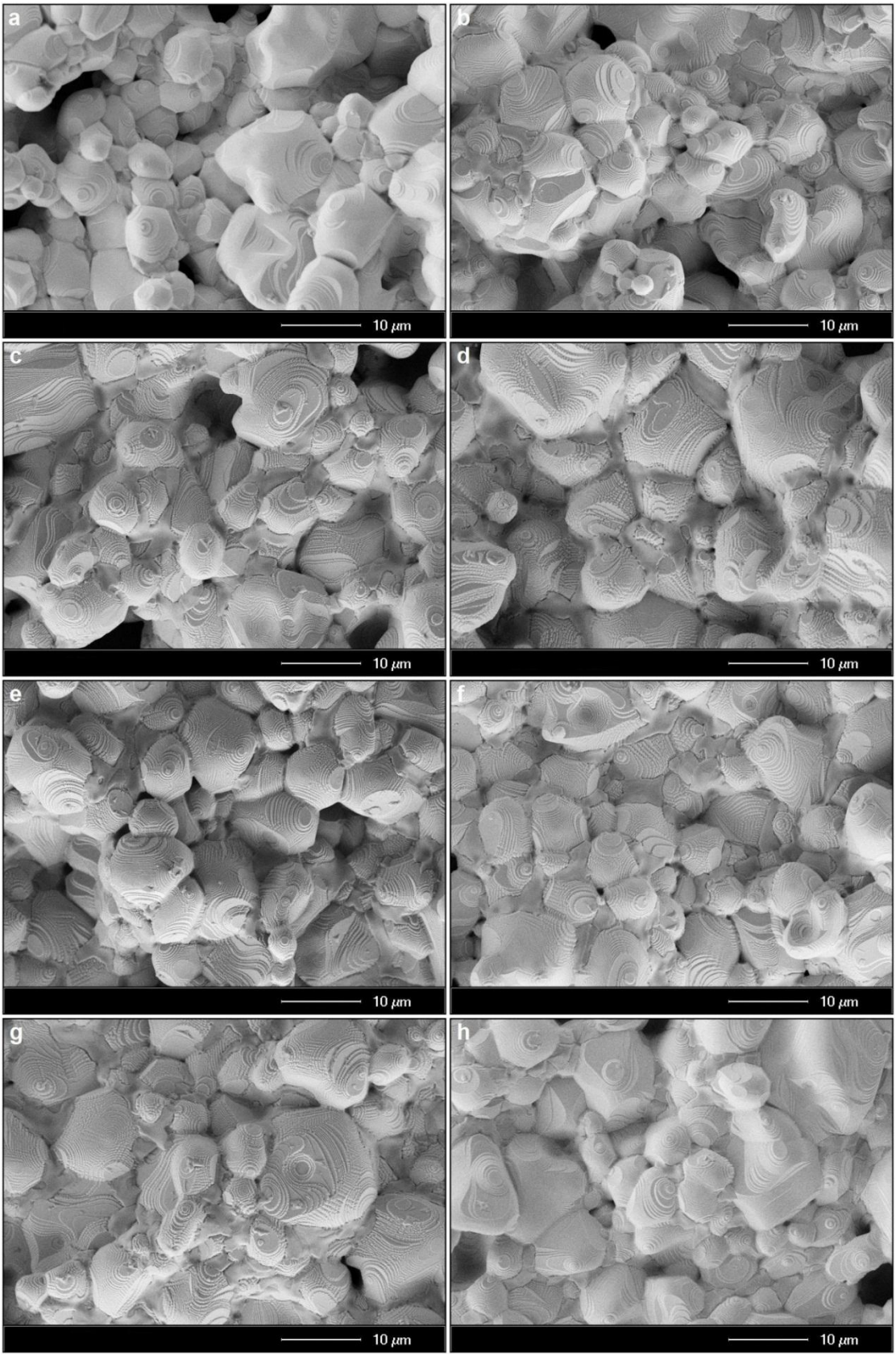

Figure 6: SEM micrographs for Eu^{3+} doped Sr_2GdTaO_6 samples; (a) undoped, (b) 0.5, (c) 1.5, (d) 3, (e) 5, (f) 7, (g) 10, (h) 20 mol% Eu^{3+}.

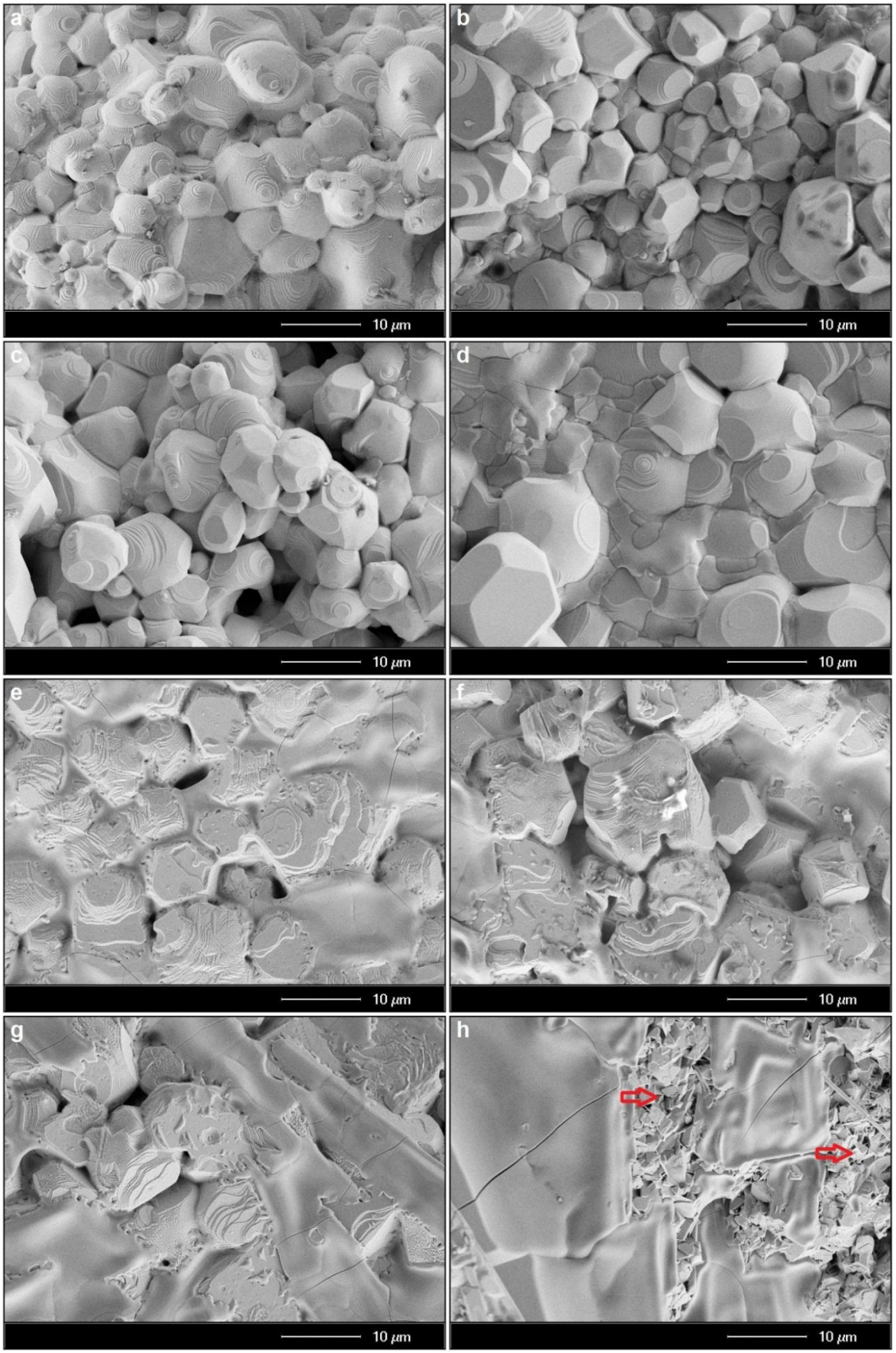

Figure 7: SEM micrographs for Eu^{3+}, B^{3+} co-doped Sr_2GdTaO_6 samples; (a) 0 (b) 5, (c) 15, (d) 30, (e) 50, (f) 70, (g) 100 mol% B^{3+}, (h) secondary phase region at 100 mol%.

Figure 6(a–h) presents SEM micrographs of the $Sr_2Gd_{1-x}Eu_xTaO_6$ series (x = 0, 0.5, 1.5, 3, 5, 7, 10, 20 mol%). The microstructure is generally dense with equiaxed, rounded to subrounded grains. Surfaces exhibit characteristic terraced step-bunching features, consistent with spiral or step-flow growth during sintering. Grain sizes are mostly in the range of ~4–13 μm, with only minor variations across the Eu^{3+} substitution series compared to the undoped sample (Figure 6a). Local intergranular porosity is present but relatively

limited, indicating effective densification under the sintering conditions.

Figure 7(a–h) shows SEM micrographs of the $Sr_2Gd_{0.9}Eu_{0.1}TaO_6$:$yB^{3+}$ series (y = 0, 5, 15, 30, 50, 70, 100 mol%), where the influence of boron concentration on microstructure is clearly evident. The undoped B^{3+} sample (y = 0, Figure 7a) exhibits relatively small, rounded grains. With increasing B^{3+} concentration (y = 5–50 mol%, Figure 7b–e), the grains undergo coarsening and adopt more faceted/polyhedral shapes. Grain sizes increase from approximately ~3–17 μm at 5–15 mol% B^{3+} to ~7–25 μm at 50 mol% B^{3+}. This trend is attributed to the flux effect of boron, which reduces the liquidus temperature at grain boundaries, enhances boundary mobility, and facilitates coarsening. At higher concentrations (y = 70–100 mol%, Figure 7f–g), the microstructure becomes more heterogeneous: exaggerated grain growth is observed in certain regions, while grain boundaries appear smoother due to partial liquid-phase wetting. In the 100 mol% B^{3+} sample (Figure 7h), fine-grained secondary regions emerge alongside the coarse grains, as indicated by the red arrow. These heterogeneous microstructural features are consistent with the appearance of secondary-phase peaks in the corresponding XRD patterns.

In summary, boron addition initially promotes grain growth and densification (up to ~50 mol% B^{3+}), leading to more uniform packing and reduced porosity. However, excessive boron levels (70 and 100 mol%) cause microstructural heterogeneity and the formation of secondary phases, which may strongly influence dielectric properties by reintroducing grain-boundary effects and defect-related conduction pathways.

3.2. Dielectric Results of Eu^{3+} Doped and Eu^{3+}, B^{3+} Co-Doped Sr_2GdTaO_6 Ceramics

The frequency-dependent dielectric responses of $Sr_2Gd_{1-x}Eu_xTaO_6$ (x = 0–20 mol%) and $Sr_2Gd_{0.9}Eu_{0.1}TaO_6$:$yB^{3+}$ (y = 0–100 mol%) ceramics are presented in Figure 8(a, b) for the dielectric constant (ε') and in Figure 9(a, b) for the dielectric loss (tan δ). Both series exhibit the typical frequency-dispersive behavior observed in perovskite-type dielectrics, characterized by high permittivity and losses at low frequencies followed by stabilization in the high-frequency regime. This behavior can be rationalized by the Maxwell–Wagner interfacial polarization mechanism and the Koop's phenomenological theory, which describes the heterogeneous dielectric response of polycrystalline ceramics, composed of semiconducting grains separated by resistive grain boundaries (46-54).

In the Eu^{3+}-doped series, the dielectric constant decreases systematically with increasing Eu^{3+} content, ranging from about 32.4 for the undoped sample to 21.8 for x = 0.20 at 20 Hz (Figure 8a). This decline in ε' can be directly correlated with the microstructural and crystallographic modifications identified in XRD and SEM analyses. XRD/W–H results (Table 1) reveal a decrease in crystallite size and an increase in microstrain, dislocation density, and stacking fault probability with increasing Eu^{3+} substitution. These features indicate lattice distortions and defect accumulation, which suppress long-range polarizability and diminish the contribution of ionic displacement to dielectric response. Complementary SEM observations (Figure 6) show only subtle grain size reductions with Eu^{3+} doping, consistent with a reduced polarizability per unit volume.

Consequently, the reduction in dielectric constant with Eu^{3+} incorporation is attributed to the combined effects of diminished crystallinity, enhanced microstrain, and weakened polarization mechanisms at both the lattice and microstructural levels. The corresponding dielectric loss (Figure 9a) also decreases with Eu^{3+} concentration, implying improved dielectric quality. This trend is consistent with the suppression of oxygen-vacancy-related leakage currents, a phenomenon widely reported in rare-earth-doped perovskites (55–62). Since Eu^{3+} is an isovalent dopant at the Gd^{3+} site, it does not directly generate charge imbalance but may stabilize oxygen stoichiometry by reducing vacancy mobility, thereby lowering conduction losses.

For the Eu^{3+}, B^{3+} co-doped ceramics, a markedly different trend is observed. The dielectric constant increases significantly with B^{3+} addition up to 50 mol%, with ε' rising from 28.3 (y = 0) to 45.7 (y = 50 mol%) at 20 Hz (Figure 8b). This enhancement is attributed to the fluxing action of boron, which promotes densification and grain coarsening, as evidenced by SEM micrographs (Figure 7). The resulting reduction in grain-boundary density lowers interfacial resistance and enhances dipolar alignment, in line with the Maxwell–Wagner polarization model. XRD/W–H data (Table 2) indicate a reduction in microstrain and defect density at moderate B^{3+} levels, confirming improved crystallinity and fewer defect-assisted conduction paths. The dielectric loss behavior (Figure 9b) supports these results: tan δ decreases steadily with B^{3+} addition up to 50 mol%, showing that grain-boundary resistance and oxygen-vacancy-related leakage currents are effectively suppressed in well-sintered, flux-assisted microstructures.

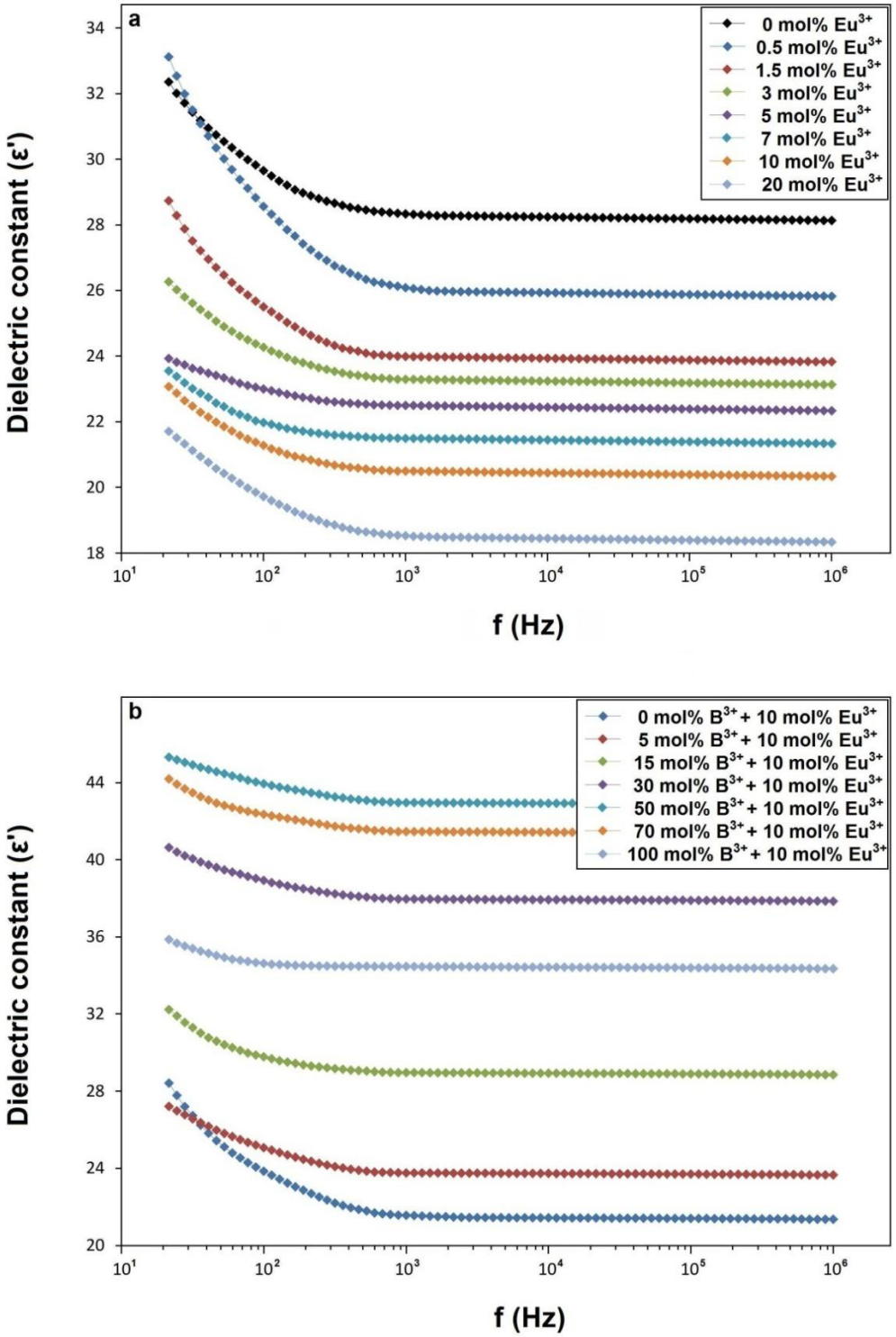

Figure 8: Frequency dependence of the dielectric constant (ε′) for (a) $Sr_2Gd_{1-x}Eu_xTaO_6$ (x = 0–20 mol%) and (b) $Sr_2Gd_{0.9}Eu_{0.1}TaO_6$:$yB^{3+}$ (y = 0–100 mol%) ceramics (ε′ decreases with Eu^{3+} doping, while moderate B^{3+} concentration enhances ε′ up to 50 mol%).

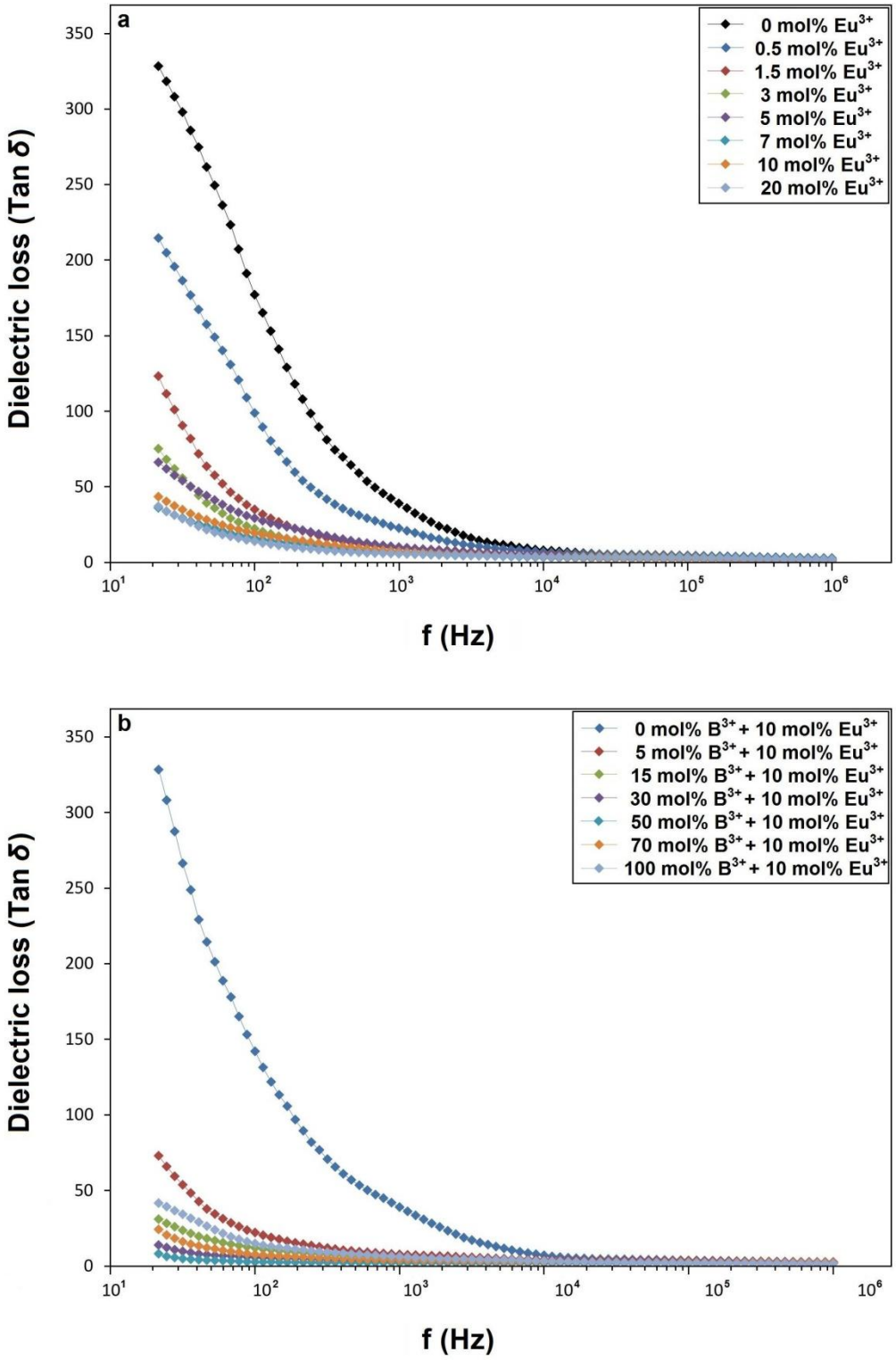

Figure 9: Frequency dependence of dielectric loss (tan δ) for (a) $Sr_2Gd_{1-x}Eu_xTaO_6$ (x = 0–20 mol%) and (b) $Sr_2Gd_{0.9}Eu_{0.1}TaO_6$:$yB^{3+}$ (y = 0–100 mol%) ceramics (tan δ decreases with Eu^{3+} and moderate B^{3+} concentrations, but slightly increases at high B^{3+} levels).

At higher B^{3+} contents (70 and 100 mol%), both ε' and tan δ deviate from these favorable trends. Although SEM reveals a continued increase in grain size, ε' decreases relative to the 50 mol% sample, and tan δ exhibits a slight upturn. This anomalous behavior arises from secondary phases detected by XRD and heterogeneous microstructures observed in SEM (Figure 7h). The crystallite-level data in Table 2 show that both Scherrer and W–H sizes decrease again, while microstrain rises sharply for ≥ 70 mol% B^{3+}. These findings suggest that excessive boron disrupts charge balance and increases lattice distortions, which enhance defect-assisted conduction and reduce dielectric performance. This explanation aligns with the results of Caruntu et al. (51), who reported that the dielectric constant scales positively with crystallite size in well-crystallized perovskites, and with Kim et al. (63), who highlighted the detrimental influence of excessive lattice strain on dielectric behavior in $BaTiO_3$ and $SrTiO_3$. Therefore, the suppression of ε' and the reappearance of tan δ at high B^{3+}

concentrations are attributed to the combined effects of secondary phase formation, strain accumulation, and enhanced oxygen-vacancy mobility in the distorted lattice. The frequency dependence further confirms these interpretations. At low frequencies (< 10^3 Hz), ε' values are higher due to space-charge polarization across grain boundaries, but dielectric losses are also more pronounced. As frequency increases, charge carriers cannot follow the alternating field, leading to a sharp decrease in both ε' and tan δ. A stable plateau is reached at high frequencies (> 10^3 Hz), where only electronic and ionic polarizations contribute. This stabilization indicates that the materials maintain relatively low dielectric losses in the technologically relevant MHz range, particularly in Eu^{3+}-substituted and moderately B^{3+}-doped compositions. This stabilization indicates that the materials maintain relatively low dielectric losses in the technologically relevant MHz range, particularly in Eu^{3+}-substituted and moderately B^{3+}-doped compositions.

Overall, the dielectric study reveals that Eu^{3+} substitution systematically reduces both ε' and tan δ by suppressing polarization and stabilizing oxygen stoichiometry, while moderate B^{3+} addition enhances ε' and minimizes tan δ through flux-assisted grain growth and defect reduction. However, excessive B^{3+} concentrations destabilize the lattice, introducing strain and secondary phases that limit dielectric performance. These correlations with XRD and SEM data highlight the crucial role of microstructural and crystallographic control in optimizing the dielectric functionality of Sr_2GdTaO_6-based ceramics.

4. CONCLUSION

In this study, the structural, microstructural, and dielectric properties of Eu^{3+}-doped and Eu^{3+}, B^{3+} co-doped Sr_2GdTaO_6 double perovskite ceramics were systematically investigated. XRD analyses confirmed monoclinic $P2_1/n$ symmetry with long-range B/B′ ordering for all compositions. Single-phase stability was preserved up to 20 mol% Eu^{3+} substitution, while boron co-doping maintained phase purity up to 70 mol%, beyond which weak secondary phases emerged. Slight peak shifts toward lower angles indicated lattice distortion arising from Eu^{3+} substitution and boron-induced structural effects. Crystallite sizes were in the range of 30–45 nm, with Eu^{3+} substitution increasing microstrain and defect density, whereas moderate B^{3+} addition reduced lattice strain through flux-assisted crystallization. SEM observations supported these findings, revealing grain refinement with Eu^{3+} doping and pronounced grain growth with boron incorporation, followed by microstructural degradation at excessive boron levels. Dielectric measurements showed a monotonic decrease in permittivity with increasing Eu^{3+} content, attributed to enhanced lattice strain and reduced polarization. In contrast, moderate boron co-doping (≤ 50 mol%) significantly enhanced the dielectric constant and suppressed dielectric loss due to grain coarsening, reduced grain-boundary density, and diminished oxygen-vacancy-related conduction. At higher boron concentrations, dielectric performance deteriorated due to strain accumulation and secondary phase formation. Frequency-dependent behavior followed the Maxwell–Wagner interfacial polarization model, with stable dielectric properties above 10^3 Hz. Overall, the results demonstrate that controlled Eu^{3+} substitution combined with optimized boron co-doping effectively tailors the lattice structure, defect chemistry, and microstructure of Sr_2GdTaO_6 ceramics, leading to enhanced dielectric performance. These findings highlight the potential of rare-earth and flux-modified double perovskites for high-permittivity dielectric components and multifunctional electronic applications.

5. CONFLICT OF INTEREST

There is no conflict of interest.

6. REFERENCES

1. Islam Z ul, Want B. Structural, optical, and dielectric properties of double perovskite $NdBaFeTiO_6$. Ceram Int [Internet]. 2025 Jan;51(2):1585–94. Available from: <URL>.

2. Feng LM, Jiang LQ, Zhu M, Liu HB, Zhou X, Li CH. Formability of ABO_3 cubic perovskites. J Phys Chem Solids [Internet]. 2008 Apr;69(4):967–74. Available from: <URL>.

3. Li J, Wang X, Cui R, Deng C. Synthesis and photoluminescence studies of novel double-perovskite phosphors, $Ba_2GdTaO_6:Eu^{3+}$ for WLEDs. Optik (Stuttg) [Internet]. 2020 Jan;201:163536. Available from: <URL>.

4. Luo Y, Chen Y, Li L, Chen J, Pang T, Chen L, et al. Three-mode fluorescence thermometers based on double perovskite $Ba_2GdNbO_6:Eu^{3+}$, Mn^{4+} phosphors. Ceram Int [Internet]. 2023 Dec;49(23):38007–14. Available from: <URL>.

5. Han B, Zhu J, Chu C, Yang X, Wang Y, Li K, et al. Sm^{3+}-Mn^{4+} activated Sr_2GdTaO_6 red phosphor for plant growth lighting and optical temperature sensing. Sensors Actuators A Phys [Internet]. 2023 Jan;349:114089. Available from: <URL>.

6. Wang L, Zhang Y, Gao D, Sha X, Chen X, Zhang Y, et al. Concentration- and temperature-dependent luminescence quenching and optical transition of Sr_2GdTaO_6: Eu^{3+} phosphor for potential applications in white LEDs. Results Phys [Internet]. 2024 Jan;56:107238. Available from: <URL>.

7. Han Y jie, Wang S, Liu H, Shi L, Zhang J ying, Zhang Z ni, et al. Synthesis and luminescent properties of a novel deep-red phosphor $Sr_2GdNbO_6:Mn^{4+}$ for indoor plant growth lighting. J Lumin [Internet]. 2020 Apr;220:116968. Available from: <URL>.

8. İlhan M, Güleryüz LF. Investigation of structural, morphological and spectral characteristics of double

perovskite Sr_2GdTaO_6 phosphors doped with Eu^{3+}, and co-doped Eu^{3+}, B^{3+} having improved quantum efficiency. J Mater Sci Mater Electron [Internet]. 2024 Dec 27;35(34):2163. Available from: <URL>.

9. Smith AJ, Welch AJE. Some mixed metal oxides of perovskite structure. Acta Crystallogr [Internet]. 1960 Aug 10;13(8):653–6. Available from: <URL>.

10. Roy R. Multiple ion substitution in the perovskite lattice. J Am Ceram Soc [Internet]. 1954 Dec 2;37(12):581–8. Available from: <URL>.

11. Chen X, Xu J, Xu Y, Luo F, Du Y. Rare earth double perovskites: A fertile soil in the field of perovskite oxides. Inorg Chem Front [Internet]. 2019;6(9):2226–38. Available from: <URL>.

12. Vasala S, Karppinen M. $A_2B'B''O_6$ perovskites: A review. Prog Solid State Chem [Internet]. 2015 May;43(1–2):1–36. Available from: <URL>.

13. Eliseeva S V., Bünzli JCG. Rare earths: Jewels for functional materials of the future. New J Chem [Internet]. 2011;35(6):1165–76. Available from: <URL>.

14. Jha AR. Rare earth materials: Properties and applications. CRC Press; 2014.

15. Mishra S, Choudhary RNP, Parida SK. A multifunctional transition metal based double perovskite $Ba_2(FeW)O_6$: Structural, microstructural, optical, electrical and ferroelectric properties. Ceram Int [Internet]. 2023 Jul;49(14):22702–17. Available from: <URL>.

16. Wang CF, Shi C, Zheng A, Wu Y, Ye L, Wang N, et al. Achieving circularly polarized luminescence and large piezoelectric response in hybrid rare-earth double perovskite by a chirality induction strategy. Mater Horizons [Internet]. 2022;9(9):2450–9. Available from: <URL>.

17. Shimizu Y, Sakagami S, Goto K, Nakachi Y, Ueda K. Tricolor luminescence in rare earth doped $CaZrO_3$ perovskite oxides. Mater Sci Eng B [Internet]. 2009 Apr;161(1–3):100–3. Available from: <URL>.

18. Parida BN, Panda N, Padhee R, Parida RK. Ferroelectric and optical behavior of $Pb_{0.5}Ba_{1.5}BiNbO_6$ double perovskite. Ferroelectrics [Internet]. 2019 Feb 17;540(1):18–28. Available from: <URL>.

19. Baral SC, Maneesha P, Rini EG, Sen S. Recent advances in LaNiMnO double perovskites for various applications; challenges and opportunities. Prog Solid State Chem [Internet]. 2023 Dec;72:100429. Available from: <URL>.

20. Wang S, Sun Q, Devakumar B, Liang J, Sun L, Huang X. Novel highly efficient and thermally stable Ca_2GdTaO_6:Eu^{3+} red-emitting phosphors with high color purity for UV/blue-excited WLEDs. J Alloys Compd [Internet]. 2019 Oct;804:93–9. Available from: <URL>.

21. Shimizu K, Kato H, Kobayashi M, Kakihana M. Synthesis and photocatalytic properties of tetragonal tungsten bronze type oxynitrides. Appl Catal B Environ [Internet]. 2017 Jun;206:444–8. Available from: <URL>.

22. Jindal S, Vasishth A, Devi S, Anand G. A review on tungsten bronze ferroelectric ceramics as electrically tunable devices. Integr Ferroelectr [Internet]. 2018 Jan 2;186(1):1–9. Available from: <URL>.

23. Bendahhou A, Marchet P, El-Houssaine A, El Barkany S, Abou-Salama M. Relationship between structural and dielectric properties of Zn-substituted $Ba_5CaTi_{2-x}Zn_xNb_8O_{30}$ tetragonal tungsten bronze. CrystEngComm [Internet]. 2021;23(1):163–73. Available from: <URL>.

24. İlhan M, Güleryüz LF, Ekmekci MK. Structural properties, photoluminescence, and judd-ofelt parameters of Eu^{3+}- doped $CoNb_2O_6$ phosphor. J Turkish Chem Soc Sect A Chem [Internet]. 2023 Aug 30;10(3):745–56. Available from: <URL>.

25. Sharma VD, Khajuria P, Khajuria A, Prakash R, Choudhary RJ. Photoluminescent and X-ray photoemission studies of Eu^{3+}-doped kosnarite $KZr_2(PO_4)_3$ nanophosphor and its Judd–Ofelt analysis. J Nanoparticle Res [Internet]. 2024 Jul 19;26(7):166. Available from: <URL>.

26. İlhan M, Keskin İÇ. Evaluation of structural behaviour, radioluminescence, Judd-Ofelt analysis and thermoluminescence kinetic parameters of Eu^{3+} doped TTB–type lead metaniobate phosphor. Phys B Condens Matter [Internet]. 2020 May;585:412106. Available from: <URL>.

27. Güleryüz LF, İlhan M. Structural, morphological, spectral properties and high quantum efficiency of Eu^{3+}, B^{3+} co-activated double perovskite Ba_2GdMO_6 (M=Nb, Ta) phosphors. Mater Sci Eng B [Internet]. 2024 Jun;304:117373. Available from: <URL>.

28. İlhan M, Keskin İÇ. Photoluminescence, radioluminescence and thermoluminescence properties of Eu^{3+} doped cadmium tantalate phosphor. Dalt Trans [Internet]. 2018;47(39):13939–48. Available from: <URL>.

29. İlhan M, Güleryüz LF. Boron doping effect on the structural, spectral properties and charge transfer mechanism of orthorhombic tungsten bronze β-$SrTa_2O_6$:Eu^{3+} phosphor. RSC Adv [Internet]. 2023;13(18):12375–85. Available from: <URL>.

30. İlhan M, Güleryüz LF, Katı Mİ. Exploring the effect of boron on the grain morphology change and spectral properties of Eu^{3+} activated barium tantalate phosphor. RSC Adv [Internet]. 2024;14(4):2687–96. Available from: <URL>.

31. İlhan M, Ekmekçi MK, Güleryüz LF. Effect of

boron incorporation on the structural, morphological, and spectral properties of $CdNb_2O_6:Dy^{3+}$ phosphor synthesized by molten salt process. Mater Sci Eng B [Internet]. 2023 Dec;298:116858. Available from: <URL>.

32. Başak AS, Ekmekçi MK, Erdem M, Ilhan M, Mergen A. Investigation of boron-doping effect on photoluminescence properties of $CdNb_2O_6$: Eu^{3+} phosphors. J Fluoresc [Internet]. 2016 Mar 11;26(2):719–24. Available from: <URL>.

33. İlhan M, Katı Mİ, Şahin N, Esmer K. Influence of boron doping on the dielectric characteristics of Eu^{3+}-doped β-$SrTa_2O_6$ and Eu^{3+}-doped $BaTa_2O_6$ tungsten bronze-type ceramics. J Electron Mater [Internet]. 2024 Oct 17;53(10):6536–52. Available from: <URL>.

34. İlhan M, Katı Mİ, Güleryüz LF. Structural and dielectric properties of RE^{3+}, B^{3+} co-doped (RE^{3+}=Sm^{3+}, Dy^{3+}) $BaTa_2O_6$ tetragonal tungsten bronze-type ceramics. J Turkish Chem Soc Sect A Chem [Internet]. 2024 Aug 30;11(3):1111–24. Available from: <URL>.

35. Zhang X, Wang B, Huang W, Chen Y, Wang G, Zeng L, et al. Synergistic boron doping of semiconductor and dielectric layers for high-performance metal oxide transistors: Interplay of experiment and theory. J Am Chem Soc [Internet]. 2018 Oct 3;140(39):12501–10. Available from: <URL>.

36. Li Z, Zhou W, Su X, Luo F, Huang Y, Wang C. Effect of boron doping on microwave dielectric properties of SiC powder synthesized by combustion synthesis. J Alloys Compd [Internet]. 2011 Jan;509(3):973–6. Available from: <URL>.

37. Mazumder R, Seal A, Sen A, Maiti HS. Effect of boron addition on the dielectric properties of giant dielectric $CaCu_3Ti_4O_{12}$. Ferroelectrics [Internet]. 2005 Oct;326(1):103–8. Available from: <URL>.

38. Keskin İÇ, Gültekin S, Katı Mİ, Türemiş M, Ay K, Arslanlar Y, et al. Structural, optical, luminescence properties and energy transfer mechanism of Tb^{3+}/Eu^{3+} co-doped $SrLa_2(MoO_4)_4$ phosphors produced by sol-gel process. J Alloys Compd [Internet]. 2019 Jun;789:932–40. Available from: <URL>.

39. Türemiş M, Keskin İÇ, Katı Mİ, Çetin A, Ay K, Kibar R. Comprehensive study on structural, thermal, morphological and luminescence (RL, PL, TL) properties of $CaLa_2(WO_4)_4$: Tb^{3+}, Dy^{3+} phosphors synthesized via sol-gel method. Ceram Int [Internet]. 2021 Sep;47(18):25708–20. Available from: <URL>.

40. Han B, Yang X, Ren J, Liu L, Zhao E, Zhu X, et al. Thermally stable deep-red emitting $Sr_2GdTaO_6:Mn^{4+}$ double perovskites for indoor plant growth LEDs. Mater Today Chem [Internet]. 2022 Mar;23:100737. Available from: <URL>.

41. Williamson G., Hall W. X-ray line broadening from filed aluminium and wolfram. Acta Metall [Internet]. 1953 Jan;1(1):22–31. Available from: <URL>.

42. Mamatha GR, Radha Krushna BR, Malleshappa J, Sharma SC, Krithika C, George A, et al. Agro-waste derived β-$Ca_2SiO_4:Nd^{3+}$ phosphors for thermal sensing and radiation dosimetry applications. Mater Sci Eng B [Internet]. 2024 Jul;305:117440. Available from: <URL>.

43. Khajuria P, Manhas M, Bedyal AK, Vij A, Swart HC, Kumar V. Structural and spectral investigation of a near-UV-converted $LiSrP_3O_9:Dy^{3+}$ phosphor for white light-emitting diodes. J Mater Sci Mater Electron [Internet]. 2022 Mar 22;33(8):6031–42. Available from: <URL>.

44. Biswas P, Kumar V, Padha N, Swart HC. Synthesis, structural and luminescence studies of $LiSrVO_4:Sm^{3+}$ nanophosphor to fill amber gap in LEDs under n-UV excitation. J Mater Sci Mater Electron [Internet]. 2017 Apr 20;28(8):6159–68. Available from: <URL>.

45. Nikam CU, Kadam SR, Shitole RS, Birajdar AP, Barote VK, Wadgnae SR, et al. Williamson-Hall and Size-strain plot based micro-structural analysis and evaluation of elastic properties of Dy^{3+} substituted Co-Zn nano-spinels. J Phys Conf Ser [Internet]. 2023 Feb 1;2426(1):012029. Available from: <URL>.

46. Wagner KW. Zur theorie der unvollkommenen dielektrika. Ann Phys [Internet]. 1913 Jan 14;345(5):817–55. Available from: <URL>.

47. Maxwell JC. A treatise on electricity and magnetism. London: Caleredon press, Oxford University; 1873.

48. Karmakar S, Mohanty HS, Behera D. Exploration of alternating current conduction mechanism and dielectric relaxation with Maxwell–Wagner effect in NiO–CdO–Gd_2O_3 nanocomposites. Eur Phys J Plus [Internet]. 2021 Oct 15;136(10):1038. Available from: <URL>.

49. Saengvong P, Chanlek N, Srepusharawoot P, Harnchana V, Thongbai P. Enhancing giant dielectric properties of Ta^{5+}-doped $Na_{1/2}Y_{1/2}Cu_3Ti_4O_{12}$ ceramics by engineering grain and grain boundary. J Am Ceram Soc [Internet]. 2022 May 15;105(5):3447–55. Available from: <URL>.

50. Samet M, Kallel A, Serghei A. Maxwell-Wagner-Sillars interfacial polarization in dielectric spectra of composite materials: Scaling laws and applications. J Compos Mater [Internet]. 2022 Aug 28;56(20):3197–217. Available from: <URL>.

51. Caruntu G, Rarig Jr R, Dumitru I, O'Connor CJ. Annealing effects on the crystallite size and dielectric properties of ultrafine $Ba_{1-x}Sr_xTiO_3$ ($0<x<1$) powders synthesized through an oxalate-complex precursor. J Mater Chem [Internet].

2006;16(8):752–8. Available from: <URL>.

52. Mahapatro J, Agrawal S. Effect of Eu^{3+} ions on electrical and dielectric properties of barium hexaferrites prepared by solution combustion method. Ceram Int [Internet]. 2021 Jul;47(14):20529–43. Available from: <URL>.

53. Evangeline T G, Annamalai A R, Ctibor P. Effect of europium addition on the microstructure and dielectric properties of CCTO ceramic prepared using conventional and microwave sintering. Molecules [Internet]. 2023 Feb 8;28(4):1649. Available from: <URL>.

54. Esha IN, Al-Amin M, Toma FTZ, Hossain E, Khan MNI, Maria KH. Synthesis and analysis of the influence of Eu^{3+} on the structural, ferromagnetic, dielectric and conductive characteristics of $Ni_{0.4}Zn_{0.45}Cu_{0.15}Fe_{(2-X)}EuxO_4$ composites using conventional double sintering ceramic method. J Ceram Process Res [Internet]. 2019 Oct;20(5):530–9. Available from: <URL>.v

55. Chandra Sati P, Arora M, Chauhan S, Kumar M, Chhoker S. Effect of Dy substitution on structural, magnetic and optical properties of $BiFeO_3$ ceramics. J Phys Chem Solids [Internet]. 2014 Jan;75(1):105–8. Available from: <URL>.

56. Chakrabarti A, Bera J. Effect of La-substitution on the structure and dielectric properties of $BaBi_4Ti_4O_{15}$ ceramics. J Alloys Compd [Internet]. 2010 Sep;505(2):668–74. Available from: <URL>.

57. İlhan M, Güleryüz LF. Evaluation of structural and dielectric properties of Eu^{3+}, B^{3+} co-doped Ba_2GdMO_6 (M=Nb, Ta) double perovskite ceramics. J Turkish Chem Soc Sect A Chem [Internet]. 2024 Aug 30;11(3):1099–110. Available from: <URL>.

58. İlhan M, Ekmekci MK, Esmer K. Structural and dielectric properties of Eu^{3+},B^{3+} co-doped $CoNb_2O_6$ ceramic. J Turkish Chem Soc Sect A Chem [Internet]. 2024 May 15;11(2):765–74. Available from: <URL>.

59. Kendall KR, Thomas JK, Loye HC. Synthesis and ionic conductivity of a new series of modified Aurivillius phases. Chem Mater [Internet]. 1995 Jan 1;7(1):50–7. Available from: <URL>.

60. Fei Liu S, Jun Wu Y, Li J, Ming Chen X. Effects of oxygen vacancies on dielectric, electrical, and ferroelectric properties of $Ba_4Nd_2Fe_2N_8O_{30}$ ceramics. Appl Phys Lett [Internet]. 2014 Feb 24;104(8):082912. Available from: <URL>.

61. Chandra Sati P, Kumar M, Chhoker S, Jewariya M. Influence of Eu substitution on structural, magnetic, optical and dielectric properties of $BiFeO_3$ multiferroic ceramics. Ceram Int [Internet]. 2015 Mar;41(2):2389–98. Available from: <URL>.

62. Ganguly P, Jha AK. Enhanced characteristics of $Ba_5SmTi_3Nb_7O_{30}$ ferroelectric nanocrystalline ceramic prepared by mechanical activation process: A comparative study. Mater Res Bull [Internet]. 2011 May;46(5):692–7. Available from: <URL>.

63. Kim L, Jung D, Kim J, Kim YS, Lee J. Strain manipulation in $BaTiO_3SrTiO_3$ artificial lattice toward high dielectric constant and its nonlinearity. Appl Phys Lett [Internet]. 2003 Mar 31;82(13):2118–20. Available from: <URL>.